

# Linköping University Post Print

## The inhomogeneous structure of water at ambient conditions

C Huang, K T Wikfeldt, T Tokushima, D Nordlund, Y Harada, U Bergmann, M Niebuhr, T M Weiss, Y Horikawa, M Leetmaa, M P Ljungberg, O Takahashi, Annika Lenz, Lars Ojamäe, A P Lyubartsev, S Shin, L G M Pettersson and A Nilsson

N.B.: When citing this work, cite the original article.

Original Publication:

C Huang, K T Wikfeldt, T Tokushima, D Nordlund, Y Harada, U Bergmann, M Niebuhr, T M Weiss, Y Horikawa, M Leetmaa, M P Ljungberg, O Takahashi, Annika Lenz, Lars Ojamäe, A P Lyubartsev, S Shin, L G M Pettersson and A Nilsson, The inhomogeneous structure of water at ambient conditions, 2009, PROCEEDINGS OF THE NATIONAL ACADEMY OF SCIENCES OF THE UNITED STATES OF AMERICA, (106), 36, 15214-15218.

<http://dx.doi.org/10.1073/pnas.0904743106>

Copyright: National Academy of Sciences

<http://www.nas.edu/>

Postprint available at: Linköping University Electronic Press

<http://urn.kb.se/resolve?urn=urn:nbn:se:liu:diva-20741>

# The Inhomogeneous Structure of Water at Ambient Conditions

Congcong Huang<sup>\*</sup>, K. T. Wikfeldt<sup>†</sup>, T. Tokushima<sup>‡</sup>, D. Nordlund<sup>\*</sup>, Y. Harada<sup>‡§</sup>, U. Bergmann<sup>\*</sup>, M. Niebuhr<sup>\*</sup>, T. M. Weiss<sup>\*</sup>, Y. Horikawa<sup>‡¶</sup>, M. Leetmaa<sup>†</sup>, M. P. Ljungberg<sup>†</sup>, O. Takahashi<sup>||</sup>, A. Lenz<sup>\*\*</sup>, L. Ojamäe<sup>\*\*</sup>, A. P. Lyubartsev<sup>††</sup>, S. Shin<sup>‡‡‡</sup>, L. G. M. Pettersson<sup>†</sup> and A. Nilsson<sup>\*†</sup>

<sup>\*</sup> Stanford Synchrotron Radiation Lightsource, P.O.B. 20450, Stanford, CA 94309, USA

<sup>†</sup> FYSIKUM, Stockholm University, AlbaNova, S-10691 Stockholm, Sweden

<sup>‡</sup> RIKEN/SPring-8, Sayo-cho, Sayo, Hyogo 679-5148, Japan

<sup>§</sup> Department of Applied Chemistry, University of Tokyo, Hongo, Bunkyo-ku, Tokyo 113-8656, Japan

<sup>¶</sup> Department of Physical Science, Hiroshima University, Higashi-Hiroshima 739-8526, Japan

<sup>||</sup> Department of Chemistry, Hiroshima University, Higashi-Hiroshima 739-8526, Japan

<sup>\*\*</sup> Department of Chemistry, Linköping University, S-581 83 Linköping, Sweden

<sup>††</sup> Division of Physical Chemistry, Stockholm University, S-10691 Stockholm, Sweden

<sup>‡‡‡</sup> Institute for Solid State Physics (ISSP), University of Tokyo, Kashiwanoha, Kashiwa, Chiba 277-8581, Japan

**Small-angle x-ray scattering (SAXS) is used to demonstrate the presence of density fluctuations in ambient water on a physical length-scale of around 1 nm; this is retained with *decreasing* temperature while the magnitude is *enhanced*. In contrast, the magnitude of fluctuations in a normal liquid, such as CCl<sub>4</sub>, exhibits no enhancement with decreasing temperature, as is also the case for water from molecular dynamics simulations under ambient conditions. Based on x-ray emission spectroscopy and x-ray Raman scattering data we propose that the density difference contrast in SAXS is due to fluctuations between tetrahedral-like and hydrogen-bond distorted structures related to, respectively, low and high density water. We combine our experimental observations to propose a model of water as a temperature-dependent, fluctuating equilibrium between the two types of local structures driven by incommensurate requirements for minimizing enthalpy (strong near-tetrahedral hydrogen-bonds) and maximizing entropy (non-directional H-bonds and disorder). The present results provide experimental evidence that the extreme differences anticipated in the hydrogen-bonding environment in the deeply supercooled regime surprisingly remain in bulk water even at conditions ranging from ambient up to close to the boiling point.**

Liquid water shows many anomalies in its thermodynamic properties such as compressibility, density variation and heat capacity (1-4). In the low-temperature regime, below the freezing point, these properties deviate strongly from normal and theories, related to a liquid-liquid phase transition between high and low density water, have been proposed to account for these anomalies (5). Although the anomalies are extreme in the supercooled region they are also present at ambient conditions where most of waters' physical, chemical and biological processes of importance occur. In contrast, water at ambient conditions has traditionally been considered as a homogeneous distribution of near-tetrahedral hydrogen-bonded (H-bonded) structures with thermal fluctuations increasing with temperature. This picture has been challenged by recent studies based on x-ray Raman (XRS) and conventional x-ray absorption spectroscopy (XAS) (6), as well as x-ray emission spectroscopy (XES) (7), suggesting two distinct local structures with tetrahedral as a minority and a highly hydrogen-bond (H-bond) distorted asymmetrical as the majority. In particular the proposed predominant asymmetrical structure has caused intense debate in the last years (see refs (7, 8) for detailed discussion).

SAXS and small-angle neutron scattering (SANS) provide the most direct probes of density variations or fluctuations on large length scales in a liquid. Through an enhancement of the structure factor at low momentum transfer,  $Q$ , small deviations from the average electron density at different length scales can be reliably identified (9). Previous SAXS studies of water have mostly focused on the supercooled region and given contradictory results where both positive (10-12) and zero enhancement (13, 14) at low  $Q$  have been reported. With the development of third-generation synchrotron light sources the ability to perform SAXS has been greatly advanced and measurements can now be performed in a large  $Q$ -range with high accuracy and reproducibility (15).

## Results

Figure 1a shows the normalized structure factor,  $S(Q)$ , derived from the SAXS intensity in ambient water ( $H_2O$ ) as function of  $Q$  for temperatures from 7 to 74 °C in the full  $Q$ -range of interest, 0.04-0.78  $\text{\AA}^{-1}$  (16). All scattering curves show an enhancement approaching  $Q = 0$  after experiencing a minimum around 0.4-0.5  $\text{\AA}^{-1}$ , which to first approximation directly indicates the presence of density heterogeneities. In particular, the

enhancement becomes *smaller* with increasing temperature in strong contrast to expectation from simple thermal density fluctuations.

In order to address if the enhancement at low  $Q$  can be related to and reproduced by thermal fluctuations in common water models, we have performed molecular dynamics (MD) simulations using the extended simple point charge (SPC/E) potential (16). The SAXS signal at low  $Q$  is given by the Fourier transform (FT) of the longer intermolecular correlations in real space from the simulation. To model SAXS data it is thus essential to use large simulation boxes (here 40,000 molecules) and also to average over long simulation runs (here longer than 0.3 ns) to reduce artificial oscillations in  $Q$  space. Figure 1b shows the SPC/E oxygen-oxygen partial structure factor,  $S(Q)$  (16). The finite size of the simulation box causes a sharp artificial increase at  $Q < 0.13 \text{ \AA}^{-1}$  in the FT. The inset shows the results for smaller simulation boxes with 5,000 molecules, where it was possible to average over significantly longer simulation times (2 ns) resulting in smoother curves, but with the FT artificial increase occurring already at  $Q = 0.25 \text{ \AA}^{-1}$  due to the smaller box size. The most important scattering enhancement observed at small  $Q$  in the experiment is completely missing from the SPC/E data even down to  $Q = 0.13 \text{ \AA}^{-1}$ . For comparison, Fig. 1c shows  $S(Q)$  of  $\text{CCl}_4$  measured at temperatures from 6 to 30 °C (16) and regarded as representing a “normal” liquid. It is clear that SAXS of  $\text{CCl}_4$  shows no temperature-dependent variation at low  $Q$ , which is observed, in contrast, in the ambient water as shown in Fig. 1a. Furthermore, the  $Q$  dependence from the SPC/E simulation is closer to the experimental data for  $\text{CCl}_4$  than for water demonstrating that the observed enhancement of the SAXS signal at low  $Q$  for water is not due to normal thermal fluctuations as obtained from standard MD simulations.

Extrapolating the structure factor in Fig. 1a to  $Q = 0$  (dashed curves) by means of a 2<sup>nd</sup> order polynomial fit to the experimental  $S(Q)$  in the range  $Q = 0.04\text{-}0.2 \text{ \AA}^{-1}$  we can relate to the isothermal compressibility,  $\chi_T$ , of water at each temperature (17) via the thermodynamical relation

$$S(0) = k_B T n \chi_T, \quad (1)$$

where  $k_B$  is the Boltzmann constant,  $T$  the absolute temperature, and  $n$  the molecular number density. We verify our SAXS data and extrapolation by comparing in Fig. 2  $\chi_T$

derived from the present SAXS data with  $\chi_T$  from an earlier study (18) measuring the velocity of sound in water; an absolute agreement is observed, confirming the quality of our data and that the density heterogeneities are related to fluctuations in the H-bonded network. If we also extrapolate the 40,000 molecules SPC/E simulations to  $Q = 0$ , we determine  $\chi_T$  as a function of temperature (Fig. 2) and find instead a linear relationship indicative of normal liquid behavior (3, 19, 20), *i.e.* without the minimum at 46 °C and increase at lower temperatures. Consistent results are obtained using an alternative estimation of  $\chi_T$  from volume fluctuations in the NPT ensemble in SPC/E simulations run for 12 ns with 7 ns equilibration time which is slightly higher but with a similar slope as a previous estimation using the NVT ensemble (21). This directly demonstrates that density fluctuations existing in a standard water model such as SPC/E do not reproduce the observed density heterogeneities that the experimental SAXS and isothermal compressibility data clearly indicate. In Fig. 2 we also compare the SPC/E results with the contribution of normal liquid behavior of water to the isothermal compressibility, as estimated from ref. (19), and find a similar temperature dependence albeit shifted in absolute value. It is thus clear that the observed fluctuations in ambient water should be different from random thermal motion and instead similar to what has been discussed in the supercooled regime (10-12).

To gain further insight we analyze the SAXS data within the framework of Ornstein-Zernicke (OZ) theory (22) assuming the density fluctuations to result from the presence of either a spinodal (23) or critical point (5). In order to apply the OZ theory we follow Conde *et al.* (19) and Kanno and Angell (20) and decompose the total scattering structure factor  $S(Q)$  into a part  $S^N(Q)$  associated with “normal liquid” behavior and an anomalous part  $S^A(Q)$  associated with critical phenomena. We assume that the “normal liquid” part of the scattering factor at  $Q = 0$ ,  $S^N(0)$ , is given by Conde’s normal contribution to the isothermal compressibility,  $\chi_T^N$ , (see Fig. 2) via Eq. (1). We further assume that the high  $Q$  region ( $>0.7 \text{ \AA}^{-1}$ ) lacks an anomalous contribution since it is dominated by near-neighbor scattering. Based on this we represent  $S^N(Q)$  by a 2<sup>nd</sup> order polynomial fitted to  $S^N(0)$  and all data points between  $Q = 0.74\text{-}0.78 \text{ \AA}^{-1}$ , as shown in

Fig. 3a. The anomalous component  $S^A(Q)$  is then obtained as the difference between the experimental data and the thus estimated  $S^N(Q)$ .

Within the OZ framework, the anomalous part is described by

$$S^A(Q) = \frac{c}{\xi^{-2} + Q^2}, \quad (2)$$

where  $\xi$  is the correlation length defined in the OZ theory and  $c$  depends on temperature but not on  $Q$  (22). In order to derive  $\xi$  we fitted  $S^A(Q)$  between  $Q = 0.04-0.19 \text{ \AA}^{-1}$  with results plotted in the top of Fig. 3b as function of temperature; the OZ correlation length is around  $3.1 \text{ \AA}$ , slowly decreasing with increasing temperature. The zero-angle anomalous structure factor,  $S^A(0) = c\xi^2$ , is, on the other hand, found to decrease more dramatically with temperature as shown in the bottom of Fig. 3b.

X-ray spectroscopies give further insight into the character of the density heterogeneities indicated by SAXS. In both XES (7) and XRS (6) it has recently been shown that there are temperature-dependent spectral changes that can be connected to the H-bonded environment. XRS corresponds to transitions from a core level to *unoccupied* states, while XES measures the decay from an *occupied* valence state to an emptied (excited) core level with the emission of an x-ray photon. Although the valence electrons are delocalized in a condensed phase, the involvement of the core level makes both XRS and XES very local probes of the electronic structure (24). Furthermore, the attosecond time scale of the XRS excitation process and the O  $1s$  life time of around 4 fs in XES (25) are much shorter than the 1-2 ps typical for H-bond dynamics (26).

The focus for our discussion will be how the experimental XES and XRS spectra of water vary with temperature and how the energy position of the spectral features relates to similar features in water vapor and ice. Figure 4a shows the temperature dependence in the lone pair  $1b_1$  region of the XES spectra for  $D_2O$  (16); using the heavier isotope minimizes core-hole induced dynamical effects on the spectral line shape (7, 27). All spectra show a split of the lone pair into two peaks, in ref. (7) denoted  $1b_1'$  and  $1b_1''$ , where the former is close in energy position to the  $1b_1$  in crystalline ice and the latter to  $1b_1$  in water vapor. The two peaks can thereby be related to tetrahedral ( $1b_1'$ ) and H-bond distorted ( $1b_1''$ ) local structures with further support for this assignment given below.

Figure 3b top part shows the temperature-dependent XRS spectra with higher energy resolution (0.5 eV) (16) compared to earlier studies (6). The spectral features in XRS and XAS of liquid water and ice have been denoted pre-edge (535 eV), main-edge (537-538 eV) and post-edge (540-541 eV) (6). Crystalline ice exhibits a strong post-edge while gas phase water has nearly all of the intensity in the pre- and main-edge regions (28).

We use energy-selective excitation to make a connection between the two x-ray spectroscopies. The XES spectra shown in Fig. 4a were all taken with excitation at 550 eV, well beyond the region with structure-dependent spectral features in the absorption spectrum. Tuning instead the energy to the specific resonant features (pre-, main- and post-edge) in the absorption spectrum makes a connection between the two x-ray spectroscopies by selecting the corresponding structural species for XES (7). This is shown in Fig. 4c where resonant XES spectra are compared with non-resonant (550 eV) XES. Normalizing the intensities to the  $1b_1''$  (distorted) peak, we find that pre-edge excitation essentially eliminates the  $1b_1'$  (tetrahedral) peak (red), excitation on the main edge gives a slight enhancement of the  $1b_1''$  (distorted) (green), while excitation on the post-edge instead enhances the  $1b_1'$  (tetrahedral) peak compared to the  $1b_1''$  (blue). Since the absorption post-edge feature in ice is much stronger than in the liquid (6), the resonant XES (blue) is consistent with that the  $1b_1'$  peak is related to tetrahedral-like species. The pre-edge peak in XRS has, on the other hand, been assigned to distorted H-bonding configurations (6, 28-32). This assignment is consistent with the observed absence of the  $1b_1'$  (tetrahedral) and the strong enhancement of the  $1b_1''$  (distorted) peak when resonantly exciting on the pre-edge feature (red).

The assignment is furthermore fully consistent with the experimentally observed temperature dependence of both XRS and XES: In XRS, the post-edge decreases and the pre-edge increases with increasing temperature (see Fig. 4b), similar to the post-edge-associated  $1b_1'$  converting to the pre-edge-associated  $1b_1''$  in XES. Hence, both XES and XRS indicate in a consistent manner that water consists of two distinct, interconverting structural species in a ratio that depends on temperature. This is also within the range of possible structures that x-ray and neutron diffraction data allow, as shown in a recent analysis using reverse Monte Carlo modeling (33).

There is another important temperature effect in the XES and XRS spectra

indicating changes beyond the interconversion of the two structural species. Both the  $1b_1''$  (distorted) peak in XES (Fig. 4a) and the related pre-edge feature in XRS (Fig. 4b) shift towards their respective gas phase position with increasing temperature while neither the  $1b_1'$  (tetrahedral) in XES nor the broad post-edge feature in XRS shows measurable changes in energy position. This implies that the distorted structural species successively become more distorted with increasing temperature through thermal excitation whereas the tetrahedral-like species do not significantly change their H-bonding. Consequently, a variation in the relative stability of the two structures with temperature is expected.

We fitted the XES spectra at each temperature into two spectral components to obtain the intensity ratio  $I_{1b_1''}/I_{1b_1'}$  between distorted and tetrahedral structures; at 25 °C we obtain  $2.5 \pm 0.5$  where the error bar is mainly due to systematic shifts based on different assumptions on the line shapes (see ref. (7) for detailed description). If the energy ( $\Delta E$ ) and entropy ( $\Delta S$ ) differences do not depend on temperature, an Arrhenius behavior is expected, i.e. a plot of the ratio,  $\ln(I_{1b_1''}/I_{1b_1'})$ , between the contributions from the two structural components to the XES spectra versus the inverse temperature ( $1/T$ ), should give a straight line with the average energy difference ( $\Delta E$ ) obtained from the slope:

$$\ln(I_{1b_1''}/I_{1b_1'}) = -\frac{\Delta E}{RT} + \frac{\Delta S}{R}. \quad (3)$$

Figure 5 plots  $\ln(I_{1b_1''}/I_{1b_1'})$  versus the inverse temperature ( $1/T$ ), where the derivative of the fitted curve is shown in the inset. We note that the data do deviate from a straight line, indicating that  $\Delta E$  and  $\Delta S$  vary with temperature between the two local structures. Since the tetrahedral structure in both XES and XRS shows little spectral change with temperature we can assume that the  $\Delta E$  and  $\Delta S$  variation are mainly attributable to changes of the distorted structure. The conversion of tetrahedral-like to distorted with temperature shows that tetrahedral-like component is of lower energy. The shifting of  $1b_1''$  position in XES and the pre-edge in XRS with temperature indicate an increase in entropy of the distorted component as it becomes thermally excited. All of these observations are consistent with that the tetrahedral structure is of lower energy - lower entropy and the distorted structure of higher energy - higher entropy.

A recent XRS study of ambient water and high density (HDA) and low density

amorphous ice (LDA) identified similarities in the liquid water spectrum with that of HDA ice (34) (see the bottom of Fig. 4b). Based on these spectra it can be hypothesized that the H-bond distorted structure, which dominates liquid water at ambient conditions, corresponds to a thermally excited and volume expanded HDA phase whereas the tetrahedral-like structures are related to LDA. The LDA spectrum can be linked to the tetrahedral structure in water through the strong post-edge seen in XRS on LDA ice and through the low energy XES  $1b_1'$  component in water with energy position close to that of crystalline ice (see Fig. 4a).

## Discussion and Conclusion

We analyze further the density fluctuations in the SAXS data in terms of the picture indicated by XES and XRS, namely that, on the time-scale of x-ray scattering, the liquid can be viewed as tetrahedral patches surrounded by thermally excited H-bond distorted structures. Although we lack information on the time-scale of the fluctuations, the attosecond interaction time of the x-ray scattering process, compared to picoseconds for H-bond dynamics, allows considering the SAXS data as an instantaneous snapshot of the structure. Since we do not detect any major contribution of intermediate structures in neither the XES nor the XRS data we make the simple approximation that the SAXS intensities are mainly connected with a density difference contrast between the two structural species seen as static on the ultrashort time scale of the scattering process. Consequently, we infer a physical picture of the derived OZ correlation length  $\xi$  (top. Fig. 3b) in terms of the radius of gyration,  $R_G$ , defined in the Guinier analysis developed for static macroparticle scattering (9). The relationship  $R_G = \sqrt{3}\xi$  (35) gives  $R_G$  decreasing from 5.6 at 7 °C to 5.1 Å at 74 °C. In order to get a sense of the physical dimensions of the tetrahedral patches we assume a spherical shape giving a diameter,  $D$ , of 14.5-13.2 Å by using the relationship  $D = 2\sqrt{5/3}R_G$  (36). In an earlier light-scattering measurement providing Raman density of states (37), a crossover frequency between the phonon and fracton regimes has been observed, suggesting the existence of low-density water patches of dimension around 10-14 Å at 22 °C, similar to the present result.

We can conclude the following experimental observations: On the time-scale of

the scattering and spectroscopic processes two local structural species coexist with tetrahedral-like patches of dimension of order 1 nm in dynamic equilibrium with H-bond distorted and thermally excited structures. Both the characteristic dimension based on SAXS and the local structure of the tetrahedral-like component based on XES/XRS are relatively insensitive to temperature whereas that of the H-bond distorted component continuously changes as it becomes thermally excited and expands, leading to loss of contrast in SAXS (bottom, Fig. 3b). Combining the SAXS and spectroscopy information we infer that the tetrahedral-like patches form as low energy-low entropy structures of lower density than the average of the liquid. The higher density, thermally excited H-bond distorted structure, on the other hand, is a high entropy structure where the higher density reduces the loss of enthalpy through a larger number of, but less specific, H-bond interactions.

The picture of ambient water presented here contains many similarities to models describing the anomalies of supercooled water based on a liquid-liquid phase transition between high and low density water (2, 4, 5). The current experimental results indicate that the liquid-liquid transition affects a larger neighborhood in the P-T phase diagram than anticipated, surprisingly extending far into the ambient regime creating an inhomogeneous fluctuating structure. In particular, the domination of the distorted structure in the liquid can be understood since high-density water is on the ambient side of the phase separation, or Widom line (38, 39) (defined as an extension of the coexistence line between low- and high-density liquid in the “one-phase region” for the second critical point scenario (5)), whereas the tetrahedral structure is on the low-temperature side. This is in line with the similar line shape seen in XRS between HDA and water at ambient conditions as shown in Fig. 4b (34) and the observation using infrared spectroscopy of a low density liquid phase in supercooled confined water at temperatures below the Widom line (40). It can furthermore be linked to the previous, much discussed Wernet *et al.* study (6), since even at room temperature the dominating high-density high-entropy structure can be expected to be highly thermally excited. This would result in much larger H-bond distortions for the distorted than for the tetrahedral component of the liquid, as suggested for the asymmetric species proposed in that study.

The detailed structure of the two types of species reported in the present work and

the time-scale on which these fluctuations exist, creating temperature-dependent density and structural heterogeneities even in ambient liquid water, are not yet precisely determined, however.

### Materials and Methods

The SAXS experiments were performed at beamline 4-2 at the Stanford Synchrotron Radiation Lightsource (SSRL) using a beam energy of 11 keV. A quantum mechanically calculated molecular scattering factor of an isolated water molecule (41) was employed to separate  $S(Q)$  from the total scattering intensity. The XRS experiments were performed at beamline 6-2 at SSRL, equipped with a Si (311) double crystal monochromator and the Raman scattering was analyzed using 14 Si (440) analyzer crystals selecting 6.46 keV photons with a resolution of  $\sim 0.3$  eV and momentum transfers of  $Q=2.6\pm 1 \text{ \AA}^{-1}$ . The O 1s XES measurements (7) were performed with a total energy resolution of 0.35 eV at BL17SU at SPring-8, Japan. Detailed description of the experimental and computational methods is described in the supporting information (16).

### Acknowledgements

Supported by the National Science Foundation (US) CHE-0809324 and CHE-0431425, the Swedish Foundation for Strategic Research, the Swedish Research Council, the Swedish National Supercomputer Center, and Japanese Ministry of Education, Science, Sports and Culture through a Grant-in-Aid for Scientific Research. Portions of this research were carried out at the Stanford Synchrotron Radiation Lightsource (SSRL), a national user facility operated by Stanford University on behalf of the U.S. Department of Energy, Office of Basic Energy Sciences. We also appreciate the critical reading of an earlier version of the manuscript by H. C. Andersen and H. Wennerström.

### References

1. Angell CA (2008) Insights into phases of liquid water from study of its unusual glass-forming properties *Science* 319: 582-587.
2. Brovchenko I, Oleinikova A (2008) Multiple Phases of Liquid Water *Chem. Phys. Chem.* 9: 2660-2675.
3. Debenedetti PG (2003) Supercooled and glassy water *J. Phys.: Condens. Matter* 15: R1669-R1726.
4. Mishima O, Stanley HE (1998) The relationship between liquid, supercooled and glassy water *Nature* 396: 329-335.
5. Poole PH, Sciortino F, Essmann U, Stanley HE (1992) Phase-Behavior of Metastable Water *Nature* 360: 324-328.
6. Wernet P, Nordlund D, Bergmann U, Cavalleri M, Odelius M, Ogasawara H, Näslund LÅ, Hirsch TK, Ojamäe L, Glatzel P, Pettersson LGM, Nilsson A (2004) The structure of the first coordination shell in liquid water *Science* 304: 995-999.
7. Tokushima T, Harada Y, Takahashi O, Senba Y, Ohashi H, Pettersson LGM, Nilsson A, Shin S (2008) High resolution x-ray emission spectroscopy of liquid water: The observation of two structural motifs *Chem. Phys. Lett.* 460: 387-400.
8. Leetmaa M, Wikfeldt KT, Ljungberg M, Odelius M, Swenson J, Nilsson A, Pettersson LGM (2008) Diffraction and IR-Raman do not prove tetrahedral water

- J. Chem. Phys.* 129: 084502.
9. Koch MHJ, Vachette P, Svergun DI (2003) Small-angle scattering: a view on the properties, structures and structural changes of biological macromolecules in solutions *Quart. Rev. BioPhys.* 36: 147.
  10. Bosio L, Teixeira J, Stanley HE (1981) Enhanced density fluctuations in supercooled H<sub>2</sub>O, D<sub>2</sub>O, and ethanol-water solutions: Evidence from small angle x-ray scattering *Phys. Rev. Lett.* 46: 597-600.
  11. Xie Y, Ludwig KF, Morales G, Hare DE, Sorensen CM (1993) Noncritical behaviour of density fluctuations in supercooled water *Phys. Rev. Lett.* 71: 2050-2053.
  12. Bosio L, Teixeira J, Bellissent-Funel MC (1989) Enhanced density fluctuations in water analyzed by neutron scattering *Phys. Rev. A* 39: 6612-6613.
  13. Dings J, Michielsen JCF, Van der Elsken J (1992) Equilibrium and nonequilibrium contributions to x-ray scattering from supercooled water *Phys. Rev. A* 45: 5731-5733.
  14. Michielsen JCF, Bot A, van der Elsken J (1988) Small-angle x-ray scattering from supercooled water *Phys. Rev. A* 38: 6439-6441.
  15. Smolsky IL, Liu P, Niebuhr M, Ito K, Weiss TM, Tsuruta H (2007) Biological small angle x-ray scattering facility at Stanford Synchrotron Radiation Laboratory *J. Appl. Cryst.* 40: 453-458.
  16. Experimental and computational methods in supporting information.
  17. Hendrick RW, Mardon PG, Shaffer LB (1974) X-Ray Zero-Angle Scattering Cross-Section of Water *J. Chem. Phys.* 61: 319-322.
  18. Kell GS (1970) Isothermal compressibility of liquid water at 1 atm *J. Chem. Eng. Data* 15: 119-122.
  19. Conde O, Teixeira J, Papon P (1982) Analysis of sound velocity in supercooled H<sub>2</sub>O, D<sub>2</sub>O, and water--ethanol mixtures *J. Chem. Phys.* 76: 3747-3753.
  20. Kanno H, Angell CA (1979) Water: Anomalous compressibilities to 1.9 kbar and correlation with supercooling limits *J. Chem. Phys.* 70: 4008-4016.
  21. Motakabbir KA, Berkowitz M (1990) Isothermal Compressibility of SPC/E Water *J. Phys. Chem.* 94: 8539-8362.
  22. Hansen JP, McDonald IR (2006) *Theory of simple liquids* (Elsevier Ltd.).
  23. Speedy RJ (1982) Stability-limit conjecture. An interpretation of the properties of water *J. Phys. Chem.* 86: 982-991.
  24. Nilsson A, Pettersson LGM (2004) Chemical bonding on surfaces probed by X-ray emission spectroscopy and density functional theory *Surf. Sci. Repts.* 55: 49-167.
  25. Neeb M, Rubensson JE, Biermann M, Eberhardt W (1994) Coherent Excitation of Vibrational Wave-Functions Observed in-Core Hole Decay Spectra of O<sub>2</sub>, N<sub>2</sub> and CO *J. El. Spec. Rel. Phenom.* 67: 261-274.
  26. Nibbering ETJ, Elsaesser T (2004) Ultrafast vibrational dynamics of hydrogen bonds in the condensed phase *Chem. Rev.* 104: 1887-1914.
  27. Fuchs O, Zharnikov M, Weinhardt L, Blum M, Weigand M, Y. Zubavichus, Bär M, Maier F, Denlinger JD, Heske C, Grunze M, Umbach E (2008) Isotope and temperature effects in liquid water probed by x-ray absorption and resonant x-ray emission spectroscopy *Phys. Rev. Lett.* 100: 027801.

28. Myneni S, Luo Y, Näslund LÅ, Cavalleri M, Ojamäe L, Ogasawara H, Pelmenchikov A, Wernet P, Väterlein P, Heske C, Hussain Z, Pettersson LGM, Nilsson A (2002) Spectroscopic probing of local hydrogen bonding structures in liquid water *J. Phys.:Condens. Matter* 14: L213-L219.
29. Iannuzzi M (2008) X-ray absorption spectra of hexagonal ice and liquid water by all-electron Gaussian and augmented plane wave calculations *J. Chem. Phys.* 128: 204506.
30. Odelius M, Cavalleri M, Nilsson A, Pettersson LGM (2006) X-ray absorption spectrum of liquid water from molecular dynamics simulations: Asymmetric model *Phys. Rev. B* 73: 024205.
31. Prendergast D, Galli G (2006) X-ray absorption spectra of water from first principles calculations *Phys. Rev. Lett.* 96: 215502.
32. Smith JD, Cappa CD, Wilson KR, Messer BM, Cohen RC, Saykally RJ (2004) Energetics of hydrogen bond network rearrangements in liquid water *Science* 306: 851-853.
33. Wikfeldt KT, Leetmaa M, Ljungberg MP, Nilsson A, Pettersson LGM (2009) On the Range of Water Structure Models Compatible with X-ray and Neutron Diffraction Data *J. Phys. Chem. B* 113: 6246-6255.
34. Tse JS, Shaw DM, Klug DD, Patchkovski S, Vanko G, Monaco G, Krisch M (2008) X-ray Raman spectroscopic study of water in the condensed phases *Phys. Rev. Lett.* 100: 095502.
35. Teixeira J (1992) in *Structure and dynamics of supramolecular aggregates and strongly interacting colloids*, eds. Chen SH, Huang JS, Tartaglia P (Kluwer, Dordrecht).
36. Guinier A, Fournet G (1955) *Small Angle Scattering of X-rays* (John Wiley & Sons, New York).
37. Majolino D, Mallamace F, Migliardo P, Aliotta F, Micali N, Vasi C (1993) Spectral evidence of connected structures in liquid water: Effective Raman density of vibrational states *Phys Rev E* 47: 2669.
38. Kumar P, Buldyrev SV, Becker SR, Poole PH, Starr FW, Stanley HE (2007) Relation between the Widom line and the breakdown of the Stokes-Einstein relation in supercooled water *Proc. National Acad. of Sci. (USA)* 104: 9575-9579.
39. Xu L, Kumar P, Buldyrev SV, Chen S-H, Poole PH, Sciortino F, Stanley HE (2005) Relation between the Widom line and the dynamic crossover in systems with a liquid-liquid phase transition *Proc. National Acad. Sci. (USA)* 102: 16558-16562.
40. Mallamace F, Broccio M, Corsaro C, Faraone A, Majolino D, Venuti V, Liu L, Mou CY, Chen SH (2007) Evidence of the existence of the low-density liquid phase in supercooled, confined water *Proc. National Acad. of Sci. (USA)* 104: 424-428.
41. Wang J, Tripathi AN, Smith JVH (1994) Chemical binding and electron correlation effects in x-ray and high energy electron scattering *J. Chem. Phys.* 101: 4842-4854.

## Figure legends

Figure 1. SAXS results for ambient and  $\text{CCl}_4$  liquid compared to SPC/E MD simulations. (a) Experimental structure factor,  $S(Q)$ , derived from small angle water scattering intensity as function of scattering momentum transfer  $Q$ . The curves, from bottom to top, correspond to increasing temperatures 7, 11, 16, 20, 25, 29, 38, 47, 56 and 74 °C. The extrapolations of scattering intensity to zero-scattering angle using a 2<sup>nd</sup> order polynomial fit at low  $Q$  are represented by dashed lines. (b) The oxygen-oxygen partial structure factor  $S(Q)$  for 5, 25, 47 and 67 °C water derived from the SPC/E model using a simulation box containing 40,000 molecules and run for 300-440 ps to reduce artificial oscillations. The mathematical properties of the FT from  $r$  to  $Q$  space prohibit observation of the behavior below  $Q = 0.13 \text{ \AA}^{-1}$  when using a box size of 106 Å. The inset shows the simulated  $S(Q)$  for ambient water from a simulation containing 5,000 water molecules run for 2 ns demonstrating the disappearance of oscillations with extended averaging; the lowest  $Q$  accessible is here  $0.25 \text{ \AA}^{-1}$ . The dashed lines indicate smooth curves where the anticipated effects of the box size and limited simulation time are removed. Note the scale of  $S(Q)$  in (b) is larger than in (a) due to steeper monotonically decaying curves for the SPC/E water in comparison to the experimental data. (c) Experimental  $S(Q)$  of  $\text{CCl}_4$  liquid as function of  $Q$ . The curves, from bottom to top, correspond to increasing temperatures 6, 11, 16, 21, 25, and 30 °C.

Figure 2. Isothermal compressibility of water,  $\chi_T$ , derived by extrapolating measured  $S(Q)$  at  $Q = 0.04\text{-}0.2 \text{ \AA}^{-1}$  to  $Q = 0 \text{ \AA}^{-1}$  (dots) compared to a previous experimental data set determined from the sound velocity in water (18) (full line). Estimated  $\chi_T$  from the SPC/E simulations (NVT ensemble) based on an extrapolation of  $S(Q)$  to  $Q = 0 \text{ \AA}^{-1}$  for the 40,000 molecule model (dashed line) and direct estimation of  $\chi_T$  for SPC/E simulations in the NPT ensemble equilibrated 7 ns and sampled over 5 ns (dotted line). The normal contribution of the isothermal compressibility,  $\chi_T^N$ , extracted from a previous experimental data set determined by the sound velocity in water-ethanol mixtures (19).

Figure 3. Ornstein-Zernicke (OZ) analysis of SAXS results of ambient water. (a) The estimation of “normal liquid” contributions,  $S^N(Q)$  (dashed lines), to the total scattering factor,  $S(Q)$  (solid lines), at 7 (black), 25 (blue) and 74 °C (red) by using the method described in the text, *i.e.*  $S^N(Q)$  is derived by fitting  $S(Q)$  between  $Q = 0.74-0.78 \text{ \AA}^{-1}$  and  $S^N(0)$  using a 2<sup>nd</sup> order polynomial function. (b) Top: OZ correlation length  $\xi$  defined in Eq. (2) as function of temperature. Bottom: the derived  $S^A(0)$  as function of temperature.

Figure 4. XES/XRS spectra of ambient water and amorphous ice. (a) The lone pair  $1b_1$  region of the O  $1s$  soft x-ray emission spectra of liquid  $D_2O$  at 10, 40, 60 and 90 °C using a non-resonant excitation energy of 550 eV. The positions of the corresponding  $1b_1$  state of crystalline ice (525.6 eV) and gas phase water (527 eV) are indicated with arrows (7). The two lone pair peaks in liquid water are denoted, respectively,  $1b_1'$ , close to the corresponding position in crystalline ice, and  $1b_1''$ , close to gas phase water. The  $1b_1'$  peak position is independent of temperature whereas the  $1b_1''$  shifts towards higher energy with increasing temperature. The spectra were normalized to give the same  $1b_1''$  peak height. The inset shows the energy difference between the  $1b_1''$  and  $1b_1'$  peaks as function of temperature. (b) Top: X-ray Raman scattering spectra of liquid  $H_2O$  at 4, 22, 60 and 90 °C normalized to have the same area. The inset magnifies the pre-edge (535 eV) spectral feature indicating a shift towards lower energy with increasing temperature. Bottom: XRS spectra of LDA and HDA ice from Ref. (34). (c) X-ray emission spectra at various excitation energies (full lines) compared to non-resonant excitation (dashed lines) at 550 eV of  $D_2O$  water at 25 °C. The inset shows the XRS spectrum of  $D_2O$  with arrows marking the corresponding excitation energies. Note that the pre-edge excited spectrum has been shifted by 0.45 eV in order to compensate for the spectator shift of a localized excited intermediate state (7).

Figure 5. Plot of the logarithm of the intensity ratio between the fitted XES spectra of  $1b_1''$  and  $1b_1'$  versus the inverse temperature,  $1/T$ . The dashed line is a guide to the eye, where the slope is not constant. The slope is shown versus temperature in the inset.

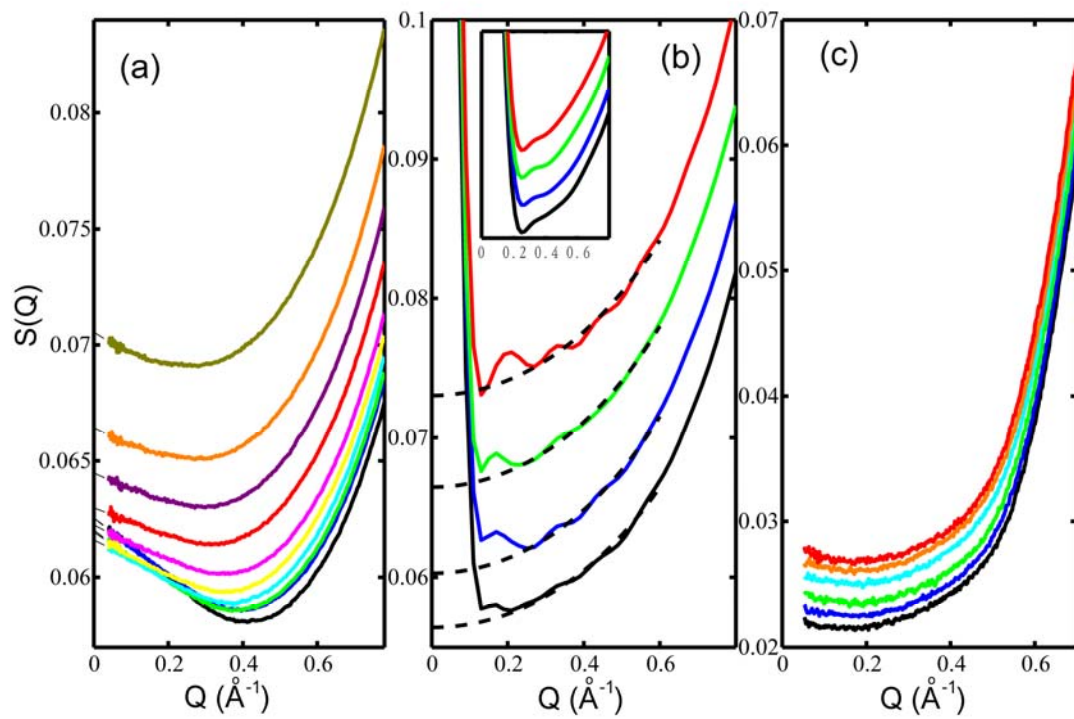


Fig. 1

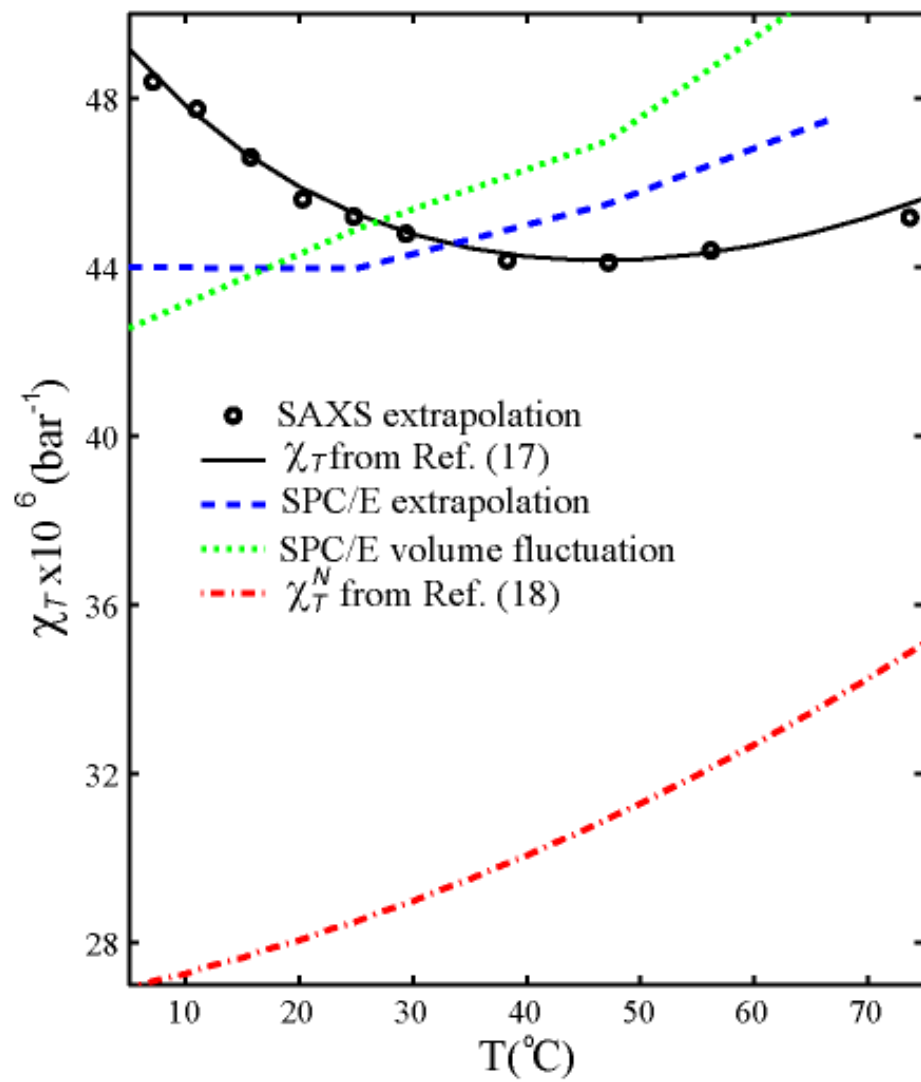


Fig. 2

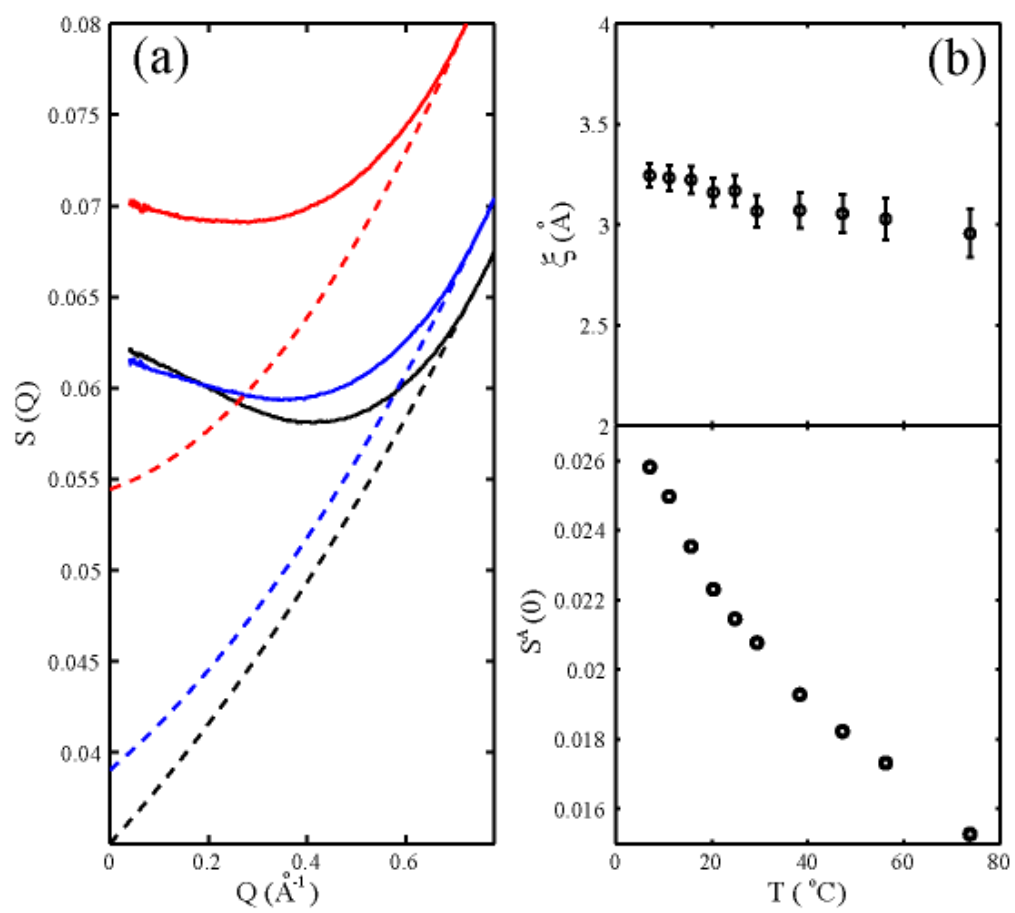


Fig. 3

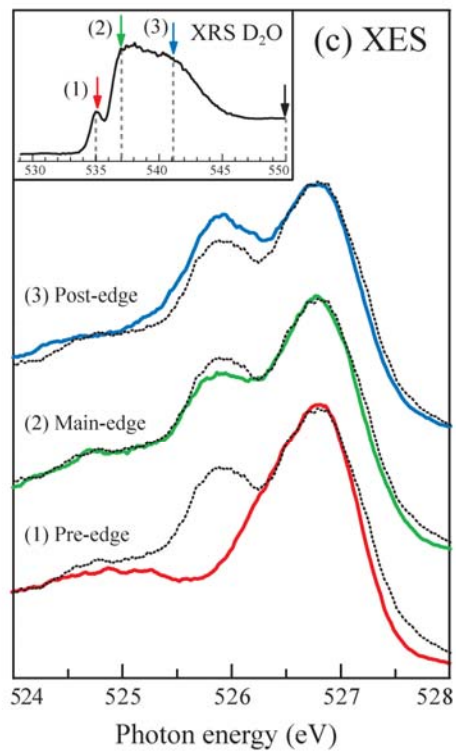
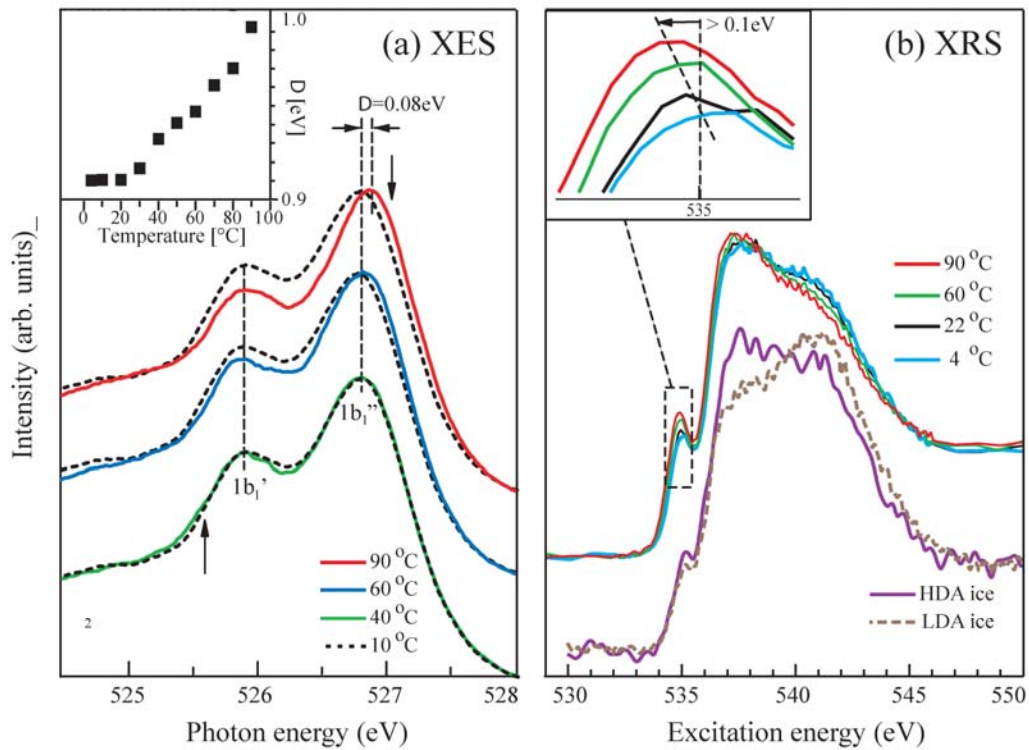


Fig. 4

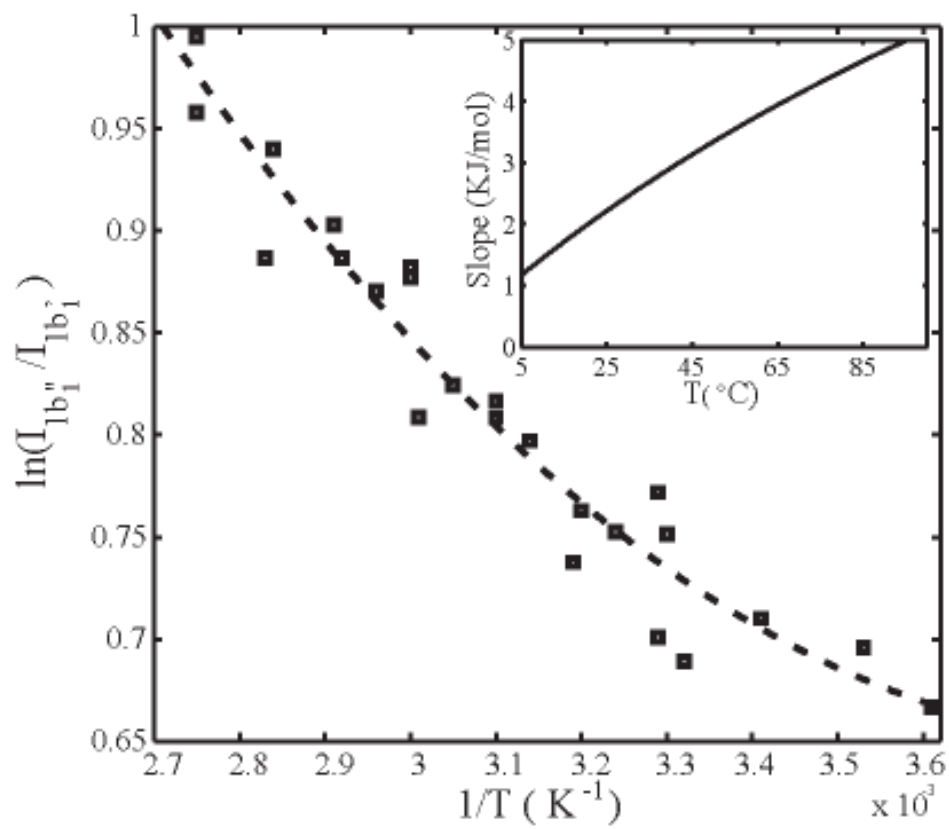


Fig. 5